Rapid Communications | Editors' Suggestion

Topological quadrupolar semimetals

Mao Lin and Taylor L. Hughes
Department of Physics and Institute for Condensed Matter Theory, University of Illinois at Urbana-Champaign, Illinois 61801, USA

(Received 30 May 2018; published 3 December 2018)

In this Rapid Communication we predict several types of topological semimetals that exhibit a bulk quadrupole moment. These semimetals are modeled with a three-dimensional extension of the two-dimensional quadrupole topological insulator. One type of semimetal has bulk nodes and gapped, topological surfaces. A second type, which we may call a higher-order topological semimetal, has a gapped bulk, but harbors a Dirac semimetal with an even number of nodes on one or more surfaces. The final type has a gapped bulk, but harbors half of a Dirac semimetal on multiple surfaces. Each of these semimetals gives rise to midgap hinge states and hinge charge, as well as surface polarization, which are all consequences of a bulk quadrupole moment. We show how the bulk quadrupole moments of these systems can be calculated from the momentum locations of bulk or surface nodes in the energy spectrum. Finally, we illustrate that in some cases it is useful to examine nodes in the Wannier bands, instead of the energy bands, to extract the bulk quadrupole moment.

DOI: 10.1103/PhysRevB.98.241103

Introduction. The recent theoretical prediction of a new class of (higher-order) topological insulators with quantized quadrupole moments [1] has opened a new direction in the field of topological phases [2–9]. The simplest quadrupole topological insulator is a two-dimensional (2D) system with an energy gap in the bulk and on the boundaries. This is unusual for topological insulators as they conventionally have characteristic gapless surface states [10,11]. However, the boundaries in the quadrupole insulator are not inert, and actually form lower-dimensional topological phases themselves. One manifestation of the surface topology is the existence of protected, midgap modes on the corners of the system where two edges intersect [1].

In this Rapid Communication we turn our attention to the prediction of classes of topological *semimetals* (TSMs) based on an extension of the quadrupole insulator to a layered three-dimensional (3D) system. These classes of TSMs include a bulk quadrupolar TSM with gapless bulk nodes, but without gapless surface modes, and several types of *higher-order* TSMs (defined below) that are gapped in the bulk, but harbor surface TSMs. Each of these 3D TSMs has a quadrupole moment that can be determined by the geometry of the bulk or surface point-node band crossings in the system; this is analogous to the electromagnetic response properties of 3D Weyl semimetals [12–17] and 2D/3D Dirac semimetals [17] which can be determined by the location of the Weyl/Dirac nodes in energy/momentum space. While we are primarily discussing these systems in the context of electronic solid state materials, we expect that they can also be straightforwardly engineered in metamaterial contexts. Topological semimetals have been designed and confirmed via spectroscopy in metamaterial systems, such as optical lattices [18,19], photonic crystals [20–24], and acoustic systems [25,26]. Given that a 2D quadrupole insulator has been realized experimentally in three independent metamaterial contexts [7–9], our proposed 3D quadrupolar semimetals are not far separated from experimental realization, and some of the predicted phenomena, especially the spectroscopic features, should be observable.

Review of quadrupole model. Let us begin by reviewing the model of a 2D topological quadrupole insulator [1]. A tight-binding representation of the Hamiltonian is illustrated in Fig. 1(a) with four spinless orbitals per unit cell, and includes inter- and intracell nearest-neighbor hopping. The Bloch Hamiltonian is

$$H(\mathbf{k}) = (\gamma_x + \lambda_x \cos k_x)\Gamma_4 + \lambda_x \sin k_x \Gamma_3 + (\gamma_y + \lambda_y \cos k_y)\Gamma_2 + \lambda_y \sin k_y \Gamma_1, \quad (1)$$

where $\Gamma_0 = \tau_3 \otimes \mathbb{I}$, $\Gamma_k = -\tau_2 \otimes \sigma_k$, $\Gamma_4 = \tau_1 \otimes \mathbb{I}$, $\mathbb{I}$ is the 2×2 identity matrix, and τ_a, σ_a are Pauli matrices with a basis specified in Fig. 1(a). γ_i and λ_i are intra- and intercell tunneling strengths. There is π flux per plaquette, and we have made a gauge choice for the relative phases of the hopping terms as shown in Fig. 1(a). For all values of γ_i and λ_i the model has x and y mirror symmetries with representation matrices $\hat{m}_x = \tau_1 \otimes \sigma_3$, and $\hat{m}_y = \tau_1 \otimes \sigma_1$. Due to the π flux, these mirror operators *anticommute*. If $|\gamma_x| = |\gamma_y|$, and $|\lambda_x| = |\lambda_y|$, then the model has C_4 rotation symmetry with the matrix representation

$$\hat{r}_4 = \begin{pmatrix} 0 & \mathbb{I} \\ -i\sigma_2 & 0 \end{pmatrix}, \quad (2)$$

where we note that $\hat{r}_4^4 = -1$ due to the π flux.

For our discussion of TSM phases it is important to understand the phase diagram of this model, shown in Fig. 2(a), as a function of the γ_i and λ_i. To simplify the discussion let us fix $\lambda_x = \lambda_y = \lambda$ from now on. The model exhibits a $\mathbb{Z}_2 \times \mathbb{Z}_2$ set of topological classes specified by the polarizations (Berry-Zak phases) (p_x, p_y) of the hybrid Wannier bands $\nu_y(k_x)$ and $\nu_x(k_y)$, respectively [27–31]. Throughout the phase diagram, the (p_x, p_y) Berry phases are quantized by the pair of x, y mirror symmetries, and take values of either 0 or $1/2$ in units of 2π. The interior (purple) square of the phase

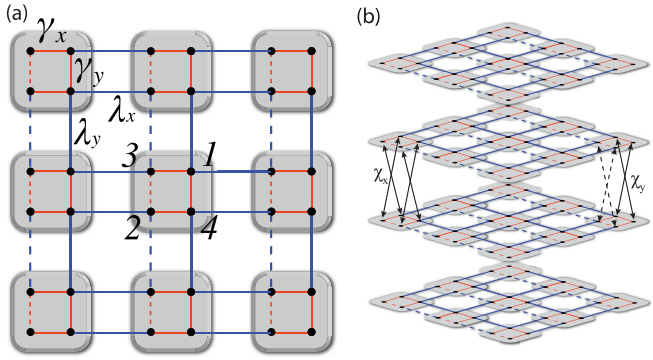

FIG. 1. (a) Tight-binding representation of the 2D topological quadrupole insulator in Eq. (1). Each black dot represents a single spinless electronic orbital. Each solid line represents a tunneling term. Each dotted line corresponds to a hopping with the same strength as a corresponding solid line, but with a relative phase of -1 which is a gauge choice that inserts a π flux in each plaquette (including within the unit cell). The ordered basis for the Γ matrices is shown on the central plaquette. (b) Stacking the 2D quadrupole insulator into a 3D system and coupling the layers to generate the TSM model Eq. (3). Note that both of the vertical coupling terms χ_x and χ_y are in every unit cell; we show them separately to avoid clutter. The dotted lines for some of the χ_y coupling terms represent a relative phase of -1 compared to the solid lines.

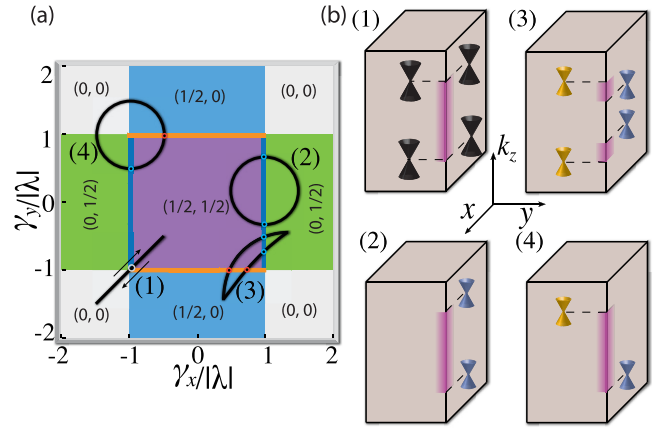

FIG. 2. (a) Phase diagram of the 2D quadrupole insulator model Eq. (1) as a function of $(\gamma_x/|\lambda|, \gamma_y/|\lambda|)$. The ordered pair in each colored region represents the $\mathbb{Z}_2 \times \mathbb{Z}_2$ topological class specified by the quantized Berry phases (p_x, p_y) of the Wannier bands. Each of the four paths represents a different type of parametrization of the TSM model in Eq. (3). (b) To each of the four paths there is an associated set of (1) bulk (1) or (2)–(4) surface gapless nodes. Note that the horizontal directions represent spatial dimensions, while the vertical direction is k_z momentum. The locations of hinge modes corresponding to each TSM configuration are highlighted on one hinge of the sample. The color of the node corresponds to the type of phase transition from which it is generated: Black nodes are bulk transitions while the blue and orange nodes correspond to transitions in the Wannier bands when passing from the $(1/2, 1/2)$ class to the $(1/2, 0)$ (orange) or $(0, 1/2)$ (blue) classes. Note that the actual path 3 parametrization used in our numerics is a degenerate line similar to path 1. We show a more open path here for illustration.

diagram represents the topological quadrupole phase having $(p_x, p_y) = (1/2, 1/2)$, which is the only region of the phase diagram with a nonvanishing quadrupole moment q_{xy}.

In addition to the mirror symmetries, the system also has C_4 symmetry along the diagonal and antidiagonal of the phase diagram. If C_4 symmetry is enforced, then there is only one type of phase transition: from the quadrupole $(1/2, 1/2)$ phase to the fully trivial phase (0,0). The transition occurs when $|\gamma| = |\lambda|$, which is accompanied by a gap closing in the *bulk* energy spectrum. When C_4 symmetry is relaxed, two other types of transitions are available. When one passes from the $(1/2, 1/2)$ phase to the $(0, 1/2)$ $[(1/2, 0)]$ phase, there will be a gap closing in the *edge* energy spectrum parallel to $\hat{x}$ $(\hat{y})$, rather than the bulk energy band, which is accompanied by a gap closing in the $\nu_y(k_x)$ $[\nu_x(k_y)]$ Wannier bands at a value of $\nu_y = 1/2$ $(\nu_x = 1/2)$ [1,3]. In contrast, transitions from the $(0, 0)$ phase to the $(1/2, 0)$ $[(0, 1/2)]$ phase have a gap closing in the hybrid-Wannier bands at a value of $\nu_y = 0$ $(\nu_x = 0)$, but there is not a generic gap-closing transition in the bulk or edge energy spectrum.

Classification of topological quadrupolar semimetals. Now let us stack the 2D quadrupole model and couple the layers to generate a Bloch Hamiltonian [see Fig. 1(b)],

$$H(\mathbf{k}) = [\gamma_x + \chi_x(k_z) + \lambda \cos k_x]\Gamma_4 + \lambda \sin k_x \Gamma_3 + [\gamma_y + \chi_y(k_z) + \lambda \cos k_y]\Gamma_2 + \lambda \sin k_y \Gamma_1, \quad (3)$$

where the $\chi_j(k_z)$ are periodic functions on the k_z Brillouin zone (BZ) determined by the choice of interlayer tunneling terms. To understand why this model can generate a TSM, consider the quantities $\gamma_i(k_z) \equiv \gamma_i + \chi_i(k_z)$, which represent maps from the k_z BZ to closed paths in the 2D phase diagram in Fig. 2(a) with a base point $(\gamma_x/|\lambda|, \gamma_y/|\lambda|)$. In Fig. 2(a) we have illustrated four different types of paths, each of which has some portion of the path within the topological quadrupole phase, and each having a discrete set of k_z at which the path is at a transition point between different topological classes. This is precisely what is needed for a TSM, and how we define a TSM, i.e., there are transition points, as a function of momentum, between different topological classes. Furthermore, for each value of k_z the system has mirror symmetries, and thus the Bloch Hamiltonian at a fixed k_z has a quantized quadrupole moment, if it is not at a transition point. Hence, the bulk quadrupole moment of each path can be straightforwardly calculated by summing up all of the values of k_z that are mapped, via the $\gamma_i(k_z)$, into the topological quadrupole region of the phase diagram. We will see below how, for each path, this calculation can be recast in terms of the momentum space locations of the transition points, analogous to, say, the calculation of the anomalous Hall coefficient in Weyl semimetals which is proportional to the momentum separation of the Weyl nodes [12–17]. Let us move on to describe the phenomenology of each path in turn.

In order to generate path (1) we need a C_4 invariant parametrization such as $\gamma_i(k_z) = -1 + 1/2\cos(k_z)$, for $i = x, y$, and $\lambda = 1$. This path passes through the C_4 invariant phase transition point when $\gamma_i(k_z) = -1$, i.e., when $k_z = \pm\pi/2$. The two bulk nodes are represented by the black cones in Fig. 2(b). The nodes represent a transition, as a function of k_z, between regions of the k_z BZ in a topological quadrupole phase, and regions in the trivial phase. We can

expand around one of the nodal points, say, $\mathbf{k} = (0, 0, \pi/2)$, to find the continuum Hamiltonian $H_{\text{node}} = \delta k_x \Gamma_3 + \delta k_y \Gamma_1 + (1/2)\delta k_z(\Gamma_2 + \Gamma_4)$. This is a gapless Dirac Hamiltonian with a fourfold degenerate Dirac point when all $\delta k_i = 0$, Adding terms proportional to Γ_0 or $(\Gamma_2 - \Gamma_4)$ will open a gap, but these terms are forbidden by a combination of mirror and C_4 symmetries. Hence, this TSM phase is protected by both mirror and C_4. Interestingly, preserving mirror but not C_4, e.g., adding $im_{13}\Gamma_1\Gamma_3$, allows for a coexisting quadrupole TSM and Weyl TSM with an anomalous Hall coefficient.

While path 1 has a similar bulk-node structure to conventional TSMs, paths 2–4 represent a completely different type of TSM, though all paths generate gapless hinge states and hence are *higher-order* TSMs. Paths 2–4 are formed in regions of the phase diagram where only the mirror symmetries are generically preserved. Let us treat paths 2 and 3 first. We can parametrize path 2 via $\gamma_x = 1 + 1/2\cos k_z$, $\gamma_y = 1/4 + 1/2\sin k_z$, and path 3 via $\gamma_x = 3/4 + 1/2\cos k_z$, $\gamma_y = -3/4 + 1/2\cos k_z$. Neither path hits a transition point where the bulk band gap closes, however, there are two and four points, for paths 2 and 3, respectively, where the Wannier bands have a gap closing when leaving the $(1/2, 1/2)$ class [see Figs. 4(a) and 4(b) for path 2]. Consequently, for path 2, when the system has open boundaries there will be two values of k_z at which the surface energy spectrum has a gap closing for surfaces normal to $\hat{y}$. Alternatively, we could have oriented path 2 so it hit one of the orange phase boundaries in Fig. 2(a), and subsequently we would find gapless nodes on surfaces normal to $\hat{x}$. Path 3 is similar to two copies of path 2, one copy with each orientation, and it will have gapless points on surfaces normal to $\hat{x}$ and $\hat{y}$ since it intersects both types of Wannier transition points as k_z traverses the BZ. Hence, these systems are gapped in the bulk, but have TSMs on their surfaces. Indeed, these systems have surface Dirac semimetals with an even number of nodes (possibly zero) on each surface normal to $\hat{x}$ and/or $\hat{y}$. The gapless nodes are protected by mirror symmetries and lie on mirror-invariant lines in the surface BZ. As an example, we take path 2 and extract the low-energy surface Hamiltonian on the surface normal to $\hat{x}$ [32]. The resulting continuum Hamiltonian, when expanded around a surface Dirac node, reads $H_{\text{surf-node}}(k_y, k_z) = vk_z\sigma_1 - \lambda k_y\sigma_2$, where v depends on the particular γ_i and λ. If we project the mirror symmetries onto the surface we find the effective representation $\hat{m}_{y,\text{eff}} = \sigma_1$, which forbids any mass terms.

Finally, let us examine path 4. This path is topologically distinct from paths 2 and 3 because it encloses a bulk critical point; hence paths 2 and 3 cannot be smoothly deformed to path 4 without closing the bulk gap. We can parametrize this path using $\gamma_x = -1 + 1/2\cos k_z$, $\gamma_y = 1 + 1/2\sin k_z$. The TSM generated on this path is perhaps the most unusual because each surface normal to $\hat{x}$ or $\hat{y}$ harbors *half* of a Dirac semimetal. This occurs because the path intersects the phase boundaries between the $(1/2, 1/2)$ class and the $(1/2, 0)$ and $(0, 1/2)$ classes just a single time each. Hence, on each surface there will only be a single node in the energy spectrum, protected by mirror symmetry, and with a similar continuum Hamiltonian to $H_{\text{surf-node}}(k)$. However, because the path intersects the phase boundaries between $(1/2, 0)$ and $(0, 0)$, and $(0, 1/2)$ and (0,0), there will be additional crossings in the Wannier bands not expressed in the energy spectrum. The structure of the Wannier band crossings is shown in Figs. 4(d) and 4(e), and interestingly this case shows spectral flow through the Wannier band values.

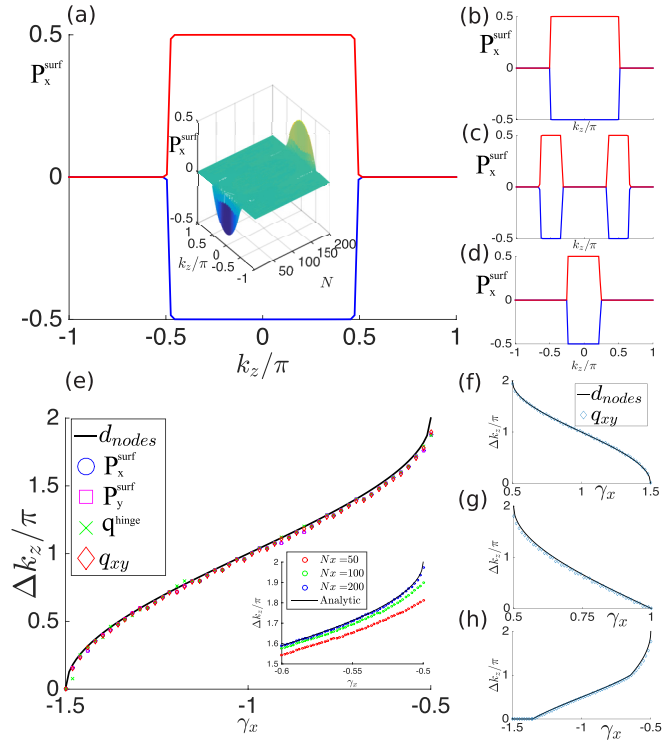

FIG. 3. Surface polarization vs k_z for paths (a) 1, (b) 2, (c) 3, and (d) 4 for a system size of 200 in the (real-space) x direction. Red and blue lines indicate polarization on opposite edges. The inset in (a) shows polarization resolved vs k_z and the spatial direction with an open boundary. (e) Comparison of nodal separation, surface polarizations [system size 100 in the (real-space) x direction], hinge charge per unit length, and quadrupole moment for path 1 as the base point is varied with $\gamma_x = \gamma_y$. Setting the electric charge $e = 1$, all quantities have units of inverse length. The inset shows scaling of the surface polarization at the upper end of the range of γ_x as system size is increased. The results converge systematically to the analytic result. (f)–(h) show comparison of nodal separation and quadrupole moment for paths 2–4, respectively, as the base points are varied with (f) $\gamma_y = 1/4$, (g) $\gamma_x = -\gamma_y$, and (h) $\gamma_x = -\gamma_y$.

Phenomenology for topological quadrupolar semimetals. To calculate the quadrupole moment of topological quadrupolar semimetals we consider the portion of the paths that lies within the topological quadrupole phase. Path 1 is similar to the usual Dirac and Weyl TSMs in that there are point nodes in the bulk spectrum. Unlike the Dirac/Weyl system, however, this TSM does not have gapless Fermi-arc surface states. Instead, the surfaces are generically gapped unless they intersect another surface at a hinge. This is a consequence of the gapped, but topological, nature of the quadrupole insulator edge states which have been stacked to form the surface states of the TSM. From our discussion above, we expect this system to have a bulk quadrupole moment $q_{xy} = \frac{e}{2\pi} b_z$, where $2b_z$ is the momentum space separation between the bulk nodes. This momentum difference precisely accounts for

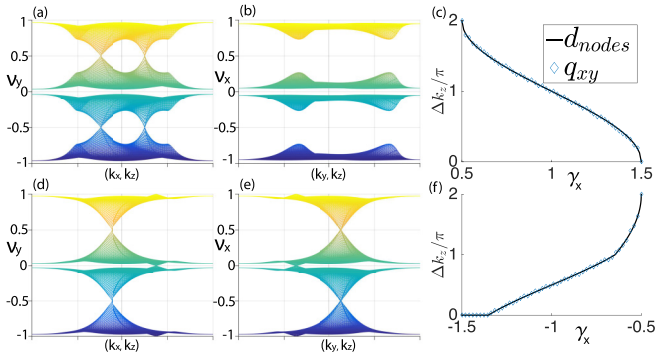

FIG. 4. Wannier bands in x and y directions calculated for (a), (b) path 2 and (d), (e) path 4 plotted vs the momenta in the transverse BZ. Note that we have used a repeated zone scheme in the Wannier value direction for clarity. Path 2 has Wannier nodes at $\nu_y = 1/2$, but no nodes in ν_x. Path 4 has nodes at $\nu_x = 0, 1/2$ and at $\nu_y = 0, 1/2$. Nodes at a Wannier value of $1/2$ have corresponding nodes in the surface energy spectrum [3]. In (c), (f) we confirm that the difference in k_z momenta of the nodes at a Wannier value of $1/2$ correctly reproduce the bulk quadrupole moment for (c) path 2 and (f) path 4 as the base points of these paths are varied identically to Figs. 3(f) and 3(h).

the portion of path 1 in the topological quadrupole region of the phase diagram. As a result, this system will exhibit a surface polarization tangent to surfaces that are normal to the x or y directions, and hinge charges/midgap bound states on hinges where the polarized surfaces intersect.

For the TSMs generated by paths 2–4, despite the bulk being completely gapped, one expects the bulk quadrupole moment to be $q_{xy} = \frac{e}{2\pi}\mathcal{B}_z$, where $2\mathcal{B}_z$ is the momentum space separation between the two surface Dirac nodes, on the same surface (path 2) or neighboring surfaces (paths 3 and 4). In Fig. 2(b) we have illustrated the hinge nodes for these configurations, and how they are cutoff by the nodal positions.

We confirm all the above results in numerical calculations in Fig. 3. In Figs. 3(a)–3(d), we show the surface polarization resolved over the k_z BZ, which is quantized to $1/2$ in the region between the bulk nodes (path 1) or surface nodes (paths 2–4). In Fig. 3(e), we shift path 1 by tuning $\gamma_x \in [-1.5, -0.5]$, while constraining $\gamma_y = \gamma_x$ and calculate the surface polarizations [3,28], hinge charge, and quadrupole moment q_{xy} [1]. We similarly calculate the quadrupole moment q_{xy} for paths 2–4 in Figs. 3(f)–3(h). We find that they all agree with the nodal separation formula above.

Wannier band calculation. So far we have evaluated the physical properties of these systems based on the locations of nodal points in the energy spectra to make contact with the extensive previous literature. However, from the argument above it is clear that one could tune the surface properties of paths 2 and 3 such that all of the surfaces are gapped, and yet there could still be a nonvanishing bulk quadrupole moment with the same magnitude (see Supplemental Material [33]). Hence, in nonideal cases where there have been modifications to the surface, and even for an ideal scenario with path 4, it may not be not obvious how to evaluate the bulk quadrupole moment using the conventional technique based on the momentum separation of energy nodes. In these cases it may be more natural to calculate the Wannier bands and use the Wannier nodal points to calculate the quadrupole moment. As a proof of concept, we performed this type of calculation for paths 2 and 4 in Fig. 4, and the results match the calculations based on the nodes in the energy spectra from Fig. 3. Specifically, we locate band crossings in the Wannier bands that occur at a value of $\nu = 1/2$, as it is precisely these crossings that are associated with band crossings in the surface energy spectra for ideal surfaces. We shifted these paths by tuning the γ_i exactly as in Fig. 3, and we find that the quadrupole moment and the momentum differences between Wannier nodal points match.

Acknowledgments. We thank W. A. Benalcazar, and B. A. Bernevig for discussions. M.L. thanks NSF Emerging Frontiers in Research and Innovation NewLAW program Grant No. EFMA-1641084 for support. T.L.H. thanks NSF CAREER Grant No. DMR-1351895 for support.

[1] W. A. Benalcazar, B. A. Bernevig, and T. L. Hughes, Science **357**, 61 (2017).
[2] Y. Peng, Y. Bao, and F. von Oppen, Phys. Rev. B **95**, 235143 (2017).
[3] W. A. Benalcazar, B. A. Bernevig, and T. L. Hughes, Phys. Rev. B **96**, 245115 (2017).
[4] Z. Song, Z. Fang, and C. Fang, Phys. Rev. Lett. **119**, 246402 (2017).
[5] F. Schindler, A. M. Cook, M. G. Vergniory, Z. Wang, S. S. P. Parkin, B. A. Bernevig, and T. Neupert, Sci. Adv. **4**, eaat0346 (2018).
[6] J. Langbehn, Y. Peng, L. Trifunovic, F. von Oppen, and P. W. Brouwer, Phys. Rev. Lett. **119**, 246401 (2017).
[7] S. Imhof, C. Berger, F. Bayer, J. Brehm, L. W. Molenkamp, T. Kiessling, F. Schindler, C. H. Lee, M. Greiter, T. Neupert, and R. Thomale, Nat. Phys. **14**, 925 (2018).
[8] M. Serra-Garcia, V. Peri, R. Süsstrunk, O. R. Bilal, T. Larsen, L. G. Villanueva, and S. D. Huber, Nature (London) **555**, 342 (2018).
[9] C. W. Peterson, W. A. Benalcazar, T. L. Hughes, and G. Bahl, Nature (London) **555**, 346 (2018).
[10] M. Z. Hasan and C. L. Kane, Rev. Mod. Phys. **82**, 3045 (2010).
[11] B. A. Bernevig and T. L. Hughes, *Topological Insulators and Topological Superconductors* (Princeton University Press, Princeton, NJ, 2013).
[12] X. Wan, A. M. Turner, A. Vishwanath, and S. Y. Savrasov, Phys. Rev. B **83**, 205101 (2011).
[13] K.-Y. Yang, Y.-M. Lu, and Y. Ran, Phys. Rev. B **84**, 075129 (2011).
[14] A. A. Burkov and L. Balents, Phys. Rev. Lett. **107**, 127205 (2011).
[15] A. A. Zyuzin and A. A. Burkov, Phys. Rev. B **86**, 115133 (2012).
[16] M. M. Vazifeh and M. Franz, Phys. Rev. Lett. **111**, 027201 (2013).
[17] S. T. Ramamurthy and T. L. Hughes, Phys. Rev. B **92**, 085105 (2015).

[18] D.-W. Zhang, S.-L. Zhu, and Z. D. Wang, Phys. Rev. A **92**, 013632 (2015).
[19] T. Dubček, C. J. Kennedy, L. Lu, W. Ketterle, M. Soljačić, and H. Buljan, Phys. Rev. Lett. **114**, 225301 (2015).
[20] B. Yang, Q. Guo, B. Tremain, R. Liu, L. E. Barr, Q. Yan, W. Gao, H. Liu, Y. Xiang, J. Chen, C. Fang, A. Hibbins, L. Lu, and S. Zhang, Science **359**, 1013 (2018).
[21] Q. Guo, B. Yang, L. Xia, W. Gao, H. Liu, J. Chen, Y. Xiang, and S. Zhang, Phys. Rev. Lett. **119**, 213901 (2017).
[22] W.-J. Chen, M. Xiao, and C. T. Chan, Nat. Commun. **7**, 13038 (2016).
[23] L. Lu, Z. Wang, D. Ye, L. Ran, L. Fu, J. D. Joannopoulos, and M. Soljačić, Science **349**, 622 (2015).
[24] L. Lu, C. Fang, L. Fu, S. G. Johnson, J. D. Joannopoulos, and M. Soljačić, Nat. Phys. **12**, 337 (2016).
[25] T. Liu, S. Zheng, H. Dai, D. Yu, and B. Xia, arXiv:1803.04284 [cond-mat.mtrl-sci].
[26] H. Ge, X. Ni, Y. Tian, S. K. Gupta, M.-H. Lu, X. Lin, W.-D. Huang, C. T. Chan, and Y.-F. Chen, Phys. Rev. Appl. **10**, 014017 (2018).
[27] A. A. Soluyanov and D. Vanderbilt, Phys. Rev. B **83**, 235401 (2011).
[28] Y. Zhou, K. M. Rabe, and D. Vanderbilt, Phys. Rev. B **92**, 041102 (2015).
[29] C. Sgiarovello, M. Peressi, and R. Resta, Phys. Rev. B **64**, 115202 (2001).
[30] S. Coh and D. Vanderbilt, Phys. Rev. Lett. **102**, 107603 (2009).
[31] R. Yu, X. L. Qi, A. Bernevig, Z. Fang, and X. Dai, Phys. Rev. B **84**, 075119 (2011).
[32] M. König, H. Buhmann, L. W. Molenkamp, T. Hughes, C.-X. Liu, X.-L. Qi, and S.-C. Zhang, J. Phys. Soc. Jpn. **77**, 031007 (2008).
[33] See Supplemental Material at http://link.aps.org/supplemental/10.1103/PhysRevB.98.241103 for topological quadrupolar semimetals.